



Research paper

# Lithium-conductive $\text{LiNbO}_3$ coated high-voltage $\text{LiNi}_{0.5}\text{Co}_{0.2}\text{Mn}_{0.3}\text{O}_2$ cathode with enhanced rate and cyclability

Haifeng Yu <sup>a,1</sup>, Shouliang Wang <sup>a,1</sup>, Yanjie Hu <sup>a</sup>, Guanjie He <sup>b</sup>, Le Quoc Bao <sup>c</sup>, Ivan P. Parkin <sup>b</sup>, Hao Jiang <sup>a,\*</sup>

<sup>a</sup> Key Laboratory for Ultrafine Materials of Ministry of Education, Shanghai Engineering Research Center of Hierarchical Nanomaterials, School of Materials Science and Engineering, East China University of Science and Technology, Shanghai 200237, China

<sup>b</sup> Christopher Ingold Laboratory, Department of Chemistry, University College London, 20 Gordon Street, London, WC1H 0AJ, UK

<sup>c</sup> Faculty of Applied Sciences, Ton Duc Thang University, 19 Nguyen Huu Tho, District 7, Ho Chi Minh City, Viet Nam

Received 9 July 2020; revised 19 August 2020; accepted 20 September 2020

Available online ■ ■ ■

## Abstract

$\text{LiNi}_{0.5}\text{Co}_{0.2}\text{Mn}_{0.3}\text{O}_2$  (NCM523) cathode materials can operate at extremely high voltages and have exceptional energy density. However, their use is limited by inherent structure instability during charge/discharge and exceptionally oxidizing  $\text{Ni}^{4+}$  at the surface. Herein, we have developed a citrate-assisted deposition concept to achieve a uniform lithium-conductive  $\text{LiNbO}_3$  coating layer on the NCM523 surface that avoids self-nucleation of Nb-contained compounds in solution reaction. The electrode–electrolyte interface is therefore stabilized by physically blocking the detrimental parasitic reactions and  $\text{Ni}^{4+}$  dissolution whilst still maintaining high  $\text{Li}^+$  conductivity. Consequently, the modified NCM523 exhibits an encouraging Li-storage specific capacity of  $207.4 \text{ mAh g}^{-1}$  at 0.2C and  $128.9 \text{ mAh g}^{-1}$  at 10C over the range 3.0–4.5 V. Additionally, a 92% capacity retention was obtained after 100 cycles at 1C, much higher than that of the pristine NCM523 (73%). This surface engineering strategy can be extended to modify other Ni-rich cathode materials with durable electrochemical performances.

© 2020, Institute of Process Engineering, Chinese Academy of Sciences. Publishing services by Elsevier B.V. on behalf of KeAi Communications Co., Ltd. This is an open access article under the CC BY-NC-ND license (<http://creativecommons.org/licenses/by-nc-nd/4.0/>).

**Keywords:** NCM523; Surface coating; Confined synthesis; Cycling stability; Li-ion batteries

## 1. Introduction

The even-increasing requirement for driving range and service life of electric vehicles has stimulated the exploitation of high-performance Li-ion batteries (LIBs) [1,2]. Because of low specific capacity and inferior durability, the cathode materials are considered to be the decisive factor that governs the performance of LIBs [3,4]. Benefiting from the synergistic effect of three elements, the  $\text{LiNi}_{0.5}\text{Co}_{0.2}\text{Mn}_{0.3}\text{O}_2$  (NCM523) layered ternary oxides display comprehensive superiorities in

terms of theoretical capacity, cost and cycle stability [5–8]. Driving the NCM cathodes to work at higher voltage ( $\geq 4.5 \text{ V}$ ) is an efficacious protocol to further enhance the energy density of LIBs [9]. Regrettably, more  $\text{Li}^+$  extracted from the layered structure at high voltage will aggravate the cation disorder and detrimental phase transition, further causing structural instability [10]. Furthermore, the enrichment of highly oxidizing  $\text{Ni}^{4+}$  will exacerbate the parasitic effect at the cathode–electrolyte interface, hence expediting the nickel ions dissolution and handicapping the transport of electrons and  $\text{Li}^+$  [11,12]. Although the overall properties of the NCM cathodes have been improved due to some rational structure engineering [13–15], the inferior endurance of NCM523 at high charging voltage is still difficult to satisfy improved performance demand.

\* Corresponding author.

E-mail address: [jianghao@ecust.edu.cn](mailto:jianghao@ecust.edu.cn) (H. Jiang).

<sup>1</sup> These authors contributed equally to this work.

<https://doi.org/10.1016/j.gee.2020.09.011>

2468-0257/© 2020, Institute of Process Engineering, Chinese Academy of Sciences. Publishing services by Elsevier B.V. on behalf of KeAi Communications Co., Ltd. This is an open access article under the CC BY-NC-ND license (<http://creativecommons.org/licenses/by-nc-nd/4.0/>).

Please cite this article as: H. Yu, S. Wang, Y. Hu et al., Lithium-conductive  $\text{LiNbO}_3$  coated high-voltage  $\text{LiNi}_{0.5}\text{Co}_{0.2}\text{Mn}_{0.3}\text{O}_2$  cathode with enhanced rate and cyclability, Green Energy & Environment, <https://doi.org/10.1016/j.gee.2020.09.011>

Numerous studies have substantiated that the failure of layered cathodes mainly starts from the interface/surface position, which make surface engineering pivotal to improving the electrochemical performances of LIBs [9,10,16]. Metal oxides (MgO, ZnO, Al<sub>2</sub>O<sub>3</sub>) [17,18], metal fluorides (AlF<sub>3</sub>) [19] and metal phosphates (AlPO<sub>4</sub>, CoPO<sub>4</sub>) [20] have been widely employed as covering layers to protect the surfaces of layered ternary cathodes, with concomitant improvement in Li-storage performances. Nevertheless, these materials always suffer from poor Li<sup>+</sup> conductivity, which increases the electrode polarization and thus reduces the rate performance [10]. The latest research has indicated that the cover layer with elevated Li<sup>+</sup> conductivity can simultaneously stabilize the electrode–electrolyte interface and accelerate the charge carrier dynamics [14,21]. For example, LiNbO<sub>3</sub> is widely used to modify the various cathode materials because of its well chemical stability and high Li<sup>+</sup> conductivity, but the commonly used solid-phase and the liquid-phase mixing methods are both difficult to obtain the uniform coating layer [22–27]. Recently, Kim et al. reported a uniform LiNbO<sub>3</sub>-coated spinel-type LiNi<sub>0.25</sub>Mn<sub>0.75</sub>O<sub>4</sub> cathode, in which the Nb-contained layer was coated on the surface of Ni<sub>0.25</sub>Mn<sub>0.75</sub>(OH)<sub>2</sub> precursors via a sol–gel method and partial Nb<sup>5+</sup> diffused into the host materials during calcination process [28]. Unfortunately, for Ni-based layered cathode, the proportion of Ni<sup>2+</sup> will increase with the excess introduction of high-valence ions due to the charge conservation, which increases the Li/Ni disorder and deteriorates the electrochemical properties [29]. Therefore, it is urgent to explore a facile uniform coating method for engineering surface of high-voltage layered NCM cathode without doping of high-valence cations to enhance the rate and cycle capabilities and meanwhile elucidate the modification mechanism.

Herein, we constructed a homogeneous LiNbO<sub>3</sub> coated NCM cathodes without changing the valence of Ni ions by a citrate-assisted deposition strategy based on the pristine NCM523 cathode materials. The intermediate cross-linking compounds by coordinating Nb<sup>5+</sup> can suppress self-nucleation and promote the realization of a uniform and tough coating layer. Furthermore, the LiNbO<sub>3</sub> with high Li<sup>+</sup> conductivity (~10<sup>-6</sup> S cm<sup>-1</sup>) can efficiently stabilize the cathode-electrolyte interface by preventing the detrimental parasitic reactions and the nickel ions dissolution, while accelerating the transfer of Li<sup>+</sup> at the interface. As a result, the modified NCM523 displays an enhanced Li-storage ability (207.4 mAh g<sup>-1</sup> at 0.2C), and a 92% capacity retention (174.3 mAh g<sup>-1</sup>) was also realized after 100 cycles at 1C. Additionally, the capacity at 10C improves from 93.2 mAh g<sup>-1</sup> to 128.9 mAh g<sup>-1</sup> after coating modification, indicating outstanding power characteristics. The LiNbO<sub>3</sub>-coated NCM523 reported in this work will promote the application of high energy density NCM cathodes with long-term life.

## 2. Experimental section

### 2.1. Preparation of LiNbO<sub>3</sub> coated LiNi<sub>0.5</sub>Co<sub>0.2</sub>Mn<sub>0.3</sub>O<sub>2</sub> cathode materials

The pristine LiNi<sub>0.5</sub>Co<sub>0.2</sub>Mn<sub>0.3</sub>O<sub>2</sub> (NCM) cathodes were supplied by BASF SE, Germany. Typically, 5 g of pristine

NCM cathodes were dispersed in 120 mL of a hybrid solution of glycol and deionized water, and 246.8 mg of ammonium citrate were dissolved in the above solution with vigorously stirring. Then, 102.5 mg of ammonium niobate oxalate and 22.3 mg of lithium acetate were added into the suspension. The mixed solution was strongly stirred at 85 °C until the solvents were thoroughly evaporated, and then the intermediates were sintered at 900 °C for 5 h to obtain the LiNbO<sub>3</sub> coated NCM cathodes with weight ratio of 1 wt% (NCM-1%LNO). The LiNbO<sub>3</sub> coated samples with weight ratio of 0.5% and 5% were also prepared, which were labeled as NCM-0.5%LNO and NCM-5%LNO, respectively. The 1 wt % LiNbO<sub>3</sub> coated NCM cathode (NCM-LNO-without citrate) without assistance of citrate was also prepared as a contrasted sample.

### 2.2. Material characterization

The crystalline phase structure was validated by X-ray diffraction (XRD, Bruker D8 Advance) with Cu K $\alpha$  radiation at scanning speed of 5° min<sup>-1</sup>. The X-ray photoelectron spectroscopy (XPS, ESCA PHI500C) with Al K $\alpha$  radiation (h $\nu$  = 1486.6 eV) was carried out to analyze the surface chemical valence states, and all of the spectra were calibrated by the C 1s peak at 284.6 eV. Scanning electron microscopy (SEM, Hitachi, S-4800) with an accelerated voltage of 15 kV was operated to observe the surface morphology. The microstructure and element distribution were surveyed by transmission electron microscopy (TEM, JEOL-2100F) at 200 kV with an accessory of X-ray energy-dispersive spectrometer (EDS). The inductively coupled plasma atomic emission spectrometer (ICP-AES, Agilent 725) was performed to research the Ni mass deposited on the Li anode.

### 2.3. Electrochemical measurements

All of the samples were assembled into coin-type 2016 cells in a glove box with filled argon to evaluate their electrochemical capabilities. The active materials, Super-P and poly(vinylidene fluoride) were evenly mixed at a mass ratio of 8:1:1 and then dispersed in N-methyl-2-pyrrolidone (NMP) solvent. After evenly stirring for 4 h, this slurry was coated on pure Al foils with loading mass of about 2.0 mg cm<sup>-2</sup> and then exsiccated at 110 °C for 15 h. The batteries were assembled by choosing the polypropylene film (Celgard 2400), and rounded Li slice as separator and anode, respectively. The electrolyte was 1.2 M LiPF<sub>6</sub> dissolved in a mixture of ethylene carbonate (EC) and ethyl methyl carbonate (EMC) with a weight ratio of 3:7. The LANDCT2001A test system was used to perform the galvanostatic charge/discharge measurements within a voltage range of 3.0–4.5 V at 0.2C–10C. Cyclic voltammogram (CV) test at a sweep speed of 0.2–1.5 mV s<sup>-1</sup> and electrochemical impedance spectra (EIS) experiment at a state of charge (4.3 V) were carried out on an Autolab PGSTAT302N. To perform post-mortem analysis, the coin cells after 100 cycles were disassembled in an Ar filled glove box. The cathode electrodes were washed by dimethyl carbonate and dried on a

heating plate of 60 °C. The Li anodes were dissolved in nitric acid and diluted by deionized water to a constant volume.

### 3. Results and discussion

Homogeneous  $\text{LiNbO}_3$  coated NCM cathodes can be synthesized via a simple citrate-assisted deposition method, as exhibited in Fig. 1a. The pristine NCM powders are evenly dispersed in a mixed solution (glycol and deionized water) containing citrate. Firstly, the citrates acted as a chelating agent will absorb on the surface of pristine NCM, then these react with the  $\text{Nb}^{5+}$  to form chelated compounds. Subsequently, cross-linking compounds containing  $\text{Nb}^{5+}$  are constructed on the surface of pristine NCM in virtue of the esterification reaction between the carboxyl groups of the citrate and the hydroxyl groups in the glycol. Finally, these compounds will *in-situ* transform to the uniform  $\text{LiNbO}_3$  coating layer after high-temperature calcination in the air. Typical XRD patterns for all samples are collectively displayed in Fig. 1b. All the main diffraction peaks are readily assignable to the hexagonal  $\alpha\text{-NaFeO}_2$  structure with space group of R-3m (JCPDS 85-1969) [30,31]. The obviously splitting of (006)/(102) and (108)/(110) peaks incontrovertibly corroborates that the  $\text{LiNbO}_3$  coating has not destroyed the crystalline structure of the host NCM cathodes [30]. Presumably because of the low thickness of the  $\text{LiNbO}_3$  layer, the

diffraction peaks for the  $\text{LiNbO}_3$  are not appeared in 0.5 wt.% and 1 wt.%  $\text{LiNbO}_3$ -coated samples. However, the typical diffraction peaks of  $\text{LiNbO}_3$  (JCPDS 74-2240) are clearly detected at the  $2\theta$  range of 20–35° in the NCM-5%LNO cathodes with greater  $\text{LiNbO}_3$  loading amount, indicating that the  $\text{LiNbO}_3$  has successfully coated the NCM cathodes. Besides, the Rietveld refinement results of the XRD patterns were also displayed in Fig. S1 and Table S1. Obviously, the almost identical unit cell parameters (a, c) and unit cell volume indicate that the  $\text{LiNbO}_3$  coating modification has no effect on the bulk crystal structure.

XPS tests of NCM-1%LNO (referred to as NCM-LNO) and pristine NCM cathodes were carried out to elucidate the influence of  $\text{LiNbO}_3$ -coated layer on chemical composition and valence state. As shown in Fig. S2, the C 1s characteristic peaks appeared at 289.8 eV are ascribed to a carbonate compound ( $\text{Li}_2\text{CO}_3$ ), which is the reaction product of the surface residual lithium salt ( $\text{Li}_2\text{O}$ ) with carbon dioxide in the air [32,33]. It was surprising that the peak intensity dramatically decreases from 24% to 16% after  $\text{LiNbO}_3$  coating, indicating an effective clean of residual lithium salts. The elimination of residual lithium salts will migrate the generation of HF in the electrolyte and improve the interfacial  $\text{Li}^+$  transfer kinetics [14]. The XPS spectra of Ni 2p (Fig. 1c) were also analyzed to research the influence of the  $\text{LiNbO}_3$  coating on the valence states for the host NCM cathodes. The deconvoluted peaks of

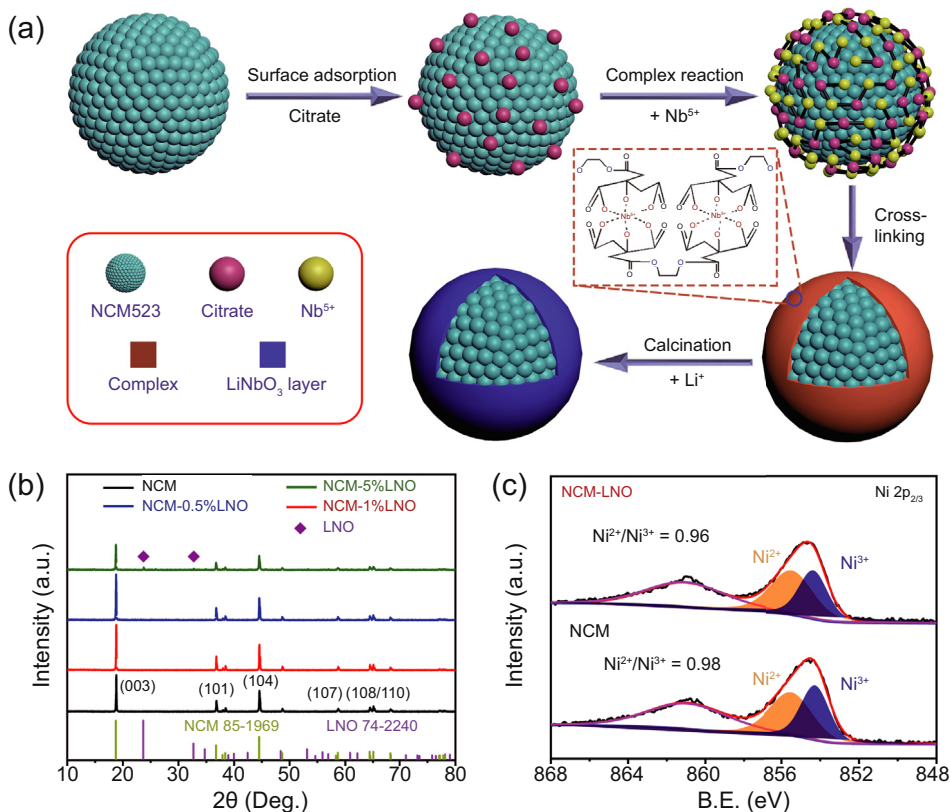


Fig. 1. (a) Schematic illustration of the fabrication process for  $\text{LiNbO}_3$  coated NCM. (b) XRD patterns of pristine NCM, NCM-0.5%LNO, NCM-1%LNO and NCM-5%LNO. (c) Ni 2p XPS patterns of the pristine NCM and NCM-LNO.

the Ni 2p<sub>3/2</sub> spectra located at 855.9 and 854.6 eV suggest the coexistence of Ni<sup>3+</sup> and Ni<sup>2+</sup> on the surface [33,34]. The intensity ratios of Ni<sup>2+</sup>/Ni<sup>3+</sup> before and after coating modification are almost identical, indicating that the coating layer has no effect on the valence states of the host materials. On account of their similar ionic radius, the Ni<sup>2+</sup> has a tendency to form antisite defects in layered structure by exchanging site with Li<sup>+</sup>, so the maintenance of valence states is beneficial to preserve the crystal structure. There is no visible skewing in the XPS spectra of Co 2p and Mn 2p (Fig. S3), implying that their valence states are also not changed after coating modification. Moreover, the resolved XPS peaks at 209.3 and 206.6 eV (Fig. S4) forcefully demonstrates that niobium ions occur on the surface of the NCM-LNO cathodes [35].

SEM and TEM techniques were also performed to investigate the surface morphology and microstructure. As shown in Fig. S5a and Fig. 2a, the NCM-LNO cathodes display micrometer-sized spherical secondary particles consisting of aggregated small primary particles of 300–500 nm, indicating that the microsphere morphology of the pristine NCM cathodes is not damaged after coating process. Moreover, the rough surface and blurred boundary are further observed under higher magnifications for NCM-LNO cathodes (Fig. 2b), which implies that the LiNbO<sub>3</sub> coating layer robustly adheres to the surface of the secondary particles. Moreover, the equably distributed Nb elements further imply that the LiNbO<sub>3</sub> is uniformly coated on the surface of NCM cathode (Fig. S6). To visibly elucidate the advantages of this citrate-assisted deposition method, the LiNbO<sub>3</sub> coated NCM cathodes (NCM-LNO-without citrate) without assistance of citrate were

also prepared and the corresponding SEM images are displayed in Fig. S7. Compared to the homogeneous surface of NCM-LNO cathodes, the small particles with irregular shape are observed on the surface of NCM-LNO-without citrate, which is caused by the self-nucleation of reactant in the solution reaction. Therefore, it is rationally concluded that the complexation action of citrate in this method can effectively avoid the self-nucleation, thus promoting the construction of homogeneous LiNbO<sub>3</sub> coating layer on the surface rather than independent small particles. The TEM analysis was also operated to further identify the LiNbO<sub>3</sub> coating and characterize the detailed crystal structure. The HRTEM image in Fig. 2c was collected from the outermost edge of the secondary particles, as shown in white rectangles in Fig. S5b. A cover layer with different lattice arrangement from the bulk material is observed on the surface, and corresponds to thicknesses of *ca* 2 nm. To further identify the crystalline states, the enlarged TEM image is provided in Fig. 2d. The interplanar spacing of 0.26 nm on the edge is attributed to the (110) planes of LiNbO<sub>3</sub> (JCPDS 74-2240), while the internal plane spacing of 0.24 nm can be indexed well to (101) planes of pristine NCM (JCPDS 85-1969). The well-defined lattices from the TEM images also imply that the LiNbO<sub>3</sub> coating has no detectable effect on the lattice structure of host NCM cathodes, which is consistent with XRD result. To determine the element distribution, EDS mapping of NCM-LNO cathodes are presented in Fig. 2e–h. The homogeneous distribution of Nb elements as well as Ni, Co and Mn elements further signify the uniformity of the LiNbO<sub>3</sub> coating layer. According to the combined results from XPS, SEM and TEM, it is shown

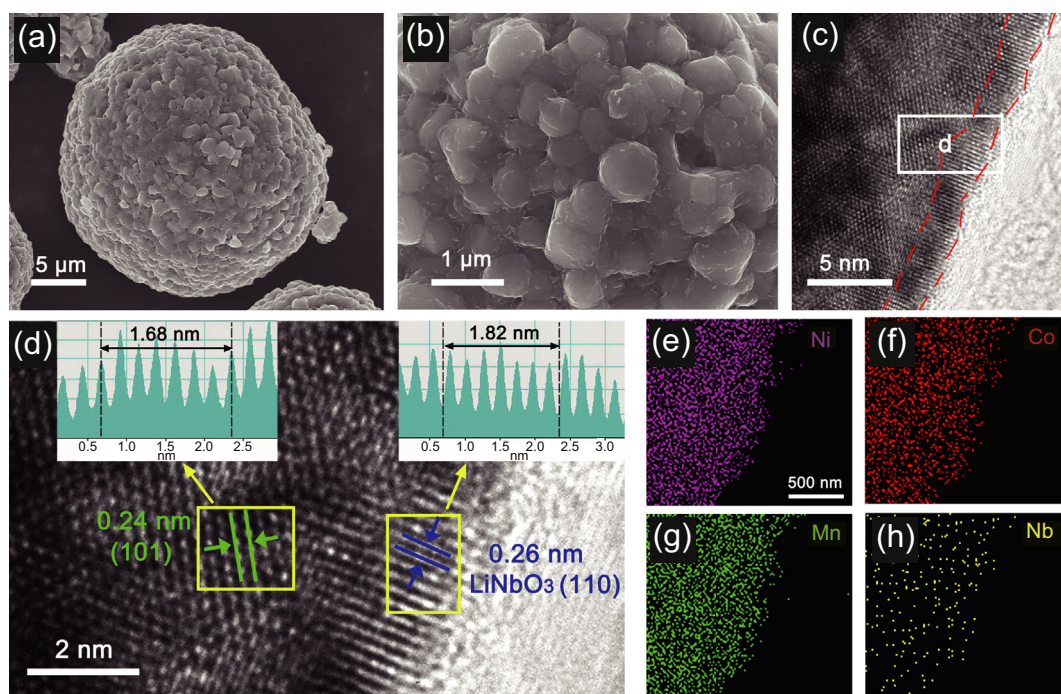


Fig. 2. (a) Low-magnification, (b) high-magnification SEM and (c) HRTEM images of the NCM-LNO. (d) Enlarged TEM image obtained from the white rectangle in part c. (e–h) EDS mapping images for Ni, Co, Mn and Nb elements.

that a uniform  $\text{LiNbO}_3$  layer has successfully realized on the surface of secondary particles in NCM cathodes.

To investigate the superiority of a  $\text{LiNbO}_3$  coating layer for lithium storage, the batteries that use these samples as cathodes were tested from 3.0 to 4.5 V at 25 °C. The first charge/discharge curves and comparison of the first discharge capacities for all the samples were shown in Fig. S8. The NCM-LNO cathodes deliver the optimal initial coulombic efficiency (85.7%) and discharge capacity (206.2  $\text{mAh g}^{-1}$ ). The rate capabilities were first investigated at various current densities (0.2C–10C) to identify the most suitable specimen (Fig. 3a). Obviously, the NCM-LNO cathodes deliver the highest specific capacity of 128.9  $\text{mAh g}^{-1}$  at 10C, while the pristine NCM cathodes only display a specific capacity of 93.2  $\text{mAh g}^{-1}$ . The discharge curves at various current densities also demonstrate smaller voltage fading for the NCM-LNO cathodes compared to pristine NCM cathodes with an increase of current density (Fig. S9). In addition, the discharge capacity of NCM-LNO cathodes can immediately recover to

201.4  $\text{mAh g}^{-1}$  when the current density decreases back to 0.2C, suggesting the superior reversibility and structure stability. It is worth noting that thin (92.5  $\text{mAh g}^{-1}$  for NCM-0.5%LNO at 10C) and thick (4  $\text{mAh g}^{-1}$  for NCM-5%LNO at 10C) coatings are not so helpful to the rate performance. Thin  $\text{LiNbO}_3$  coating layers cannot effectively wipe off the residual lithium salts and completely cover the particles, so the improvement for  $\text{Li}^+$  transfer kinetics is finite. The introduction of thick  $\text{LiNbO}_3$  coatings with low electron conductivity will hinder the transfer of electron at the interface and further sacrifice the rate capability, although the  $\text{Li}^+$  transfer rate can be improved. Moreover, the rate performance of NCM-LNO-without citrate were also shown to illustrate the effect of citrate-assisted deposition strategy for electrochemical performance. The NCM-LNO-without citrate deliver a lower specific capacity of 118.7  $\text{mAh g}^{-1}$  at 10C, which is due to that the inferior uniformity of the  $\text{LiNbO}_3$  coating layer will obstruct the enhancement of electrochemical dynamics. Besides rate capability, the cycle durability of batteries is also a

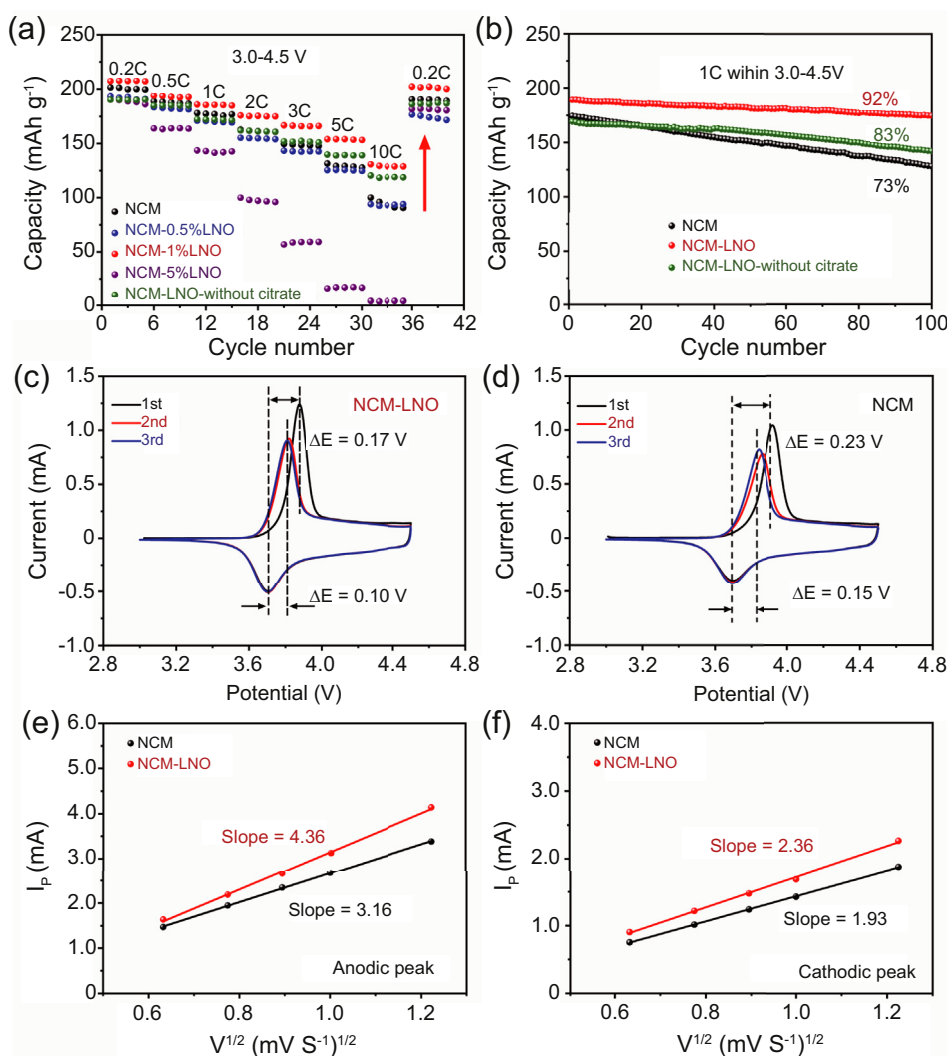


Fig. 3. (a) Rate capability and (b) cycle stability of the modified and pristine NCM. (c, d) The initial three CV curves in 3.0–4.5 V at a sweep speed of  $0.2 \text{ mV s}^{-1}$  and (e, f) linear relationship between anodic/cathodic peak current ( $i_p$ ) and the square root of the scan rate ( $v^{1/2}$ ) for the NCM-LNO and pristine NCM.

key parameter affecting their practical availability. As displayed in Fig. 3b, a high reversible capacity ( $174.3 \text{ mA h g}^{-1}$ ) is still maintained (capacity retention ratio of 92%) for NCM-LNO cathodes even after 100 cycles at 1C. In comparison, a dramatic capacity fade is observed for the pristine NCM cathodes, which only retain 73% capacity after 100 cycles (from  $174.6 \text{ mAh g}^{-1}$  to  $127.0 \text{ mAh g}^{-1}$ ). Due to the incomplete and uneven coating layer, the capacity retention ratio of NCM-LNO-without citrate only improves to 83%. The variation trend of capacity and voltage platform during 100 cycles were observed in homologous charge/discharge curves (Fig. S10). Clearly, the NCM-LNO cathodes show inappreciable voltage decline and less capacity loss, which matches well with the superior cycle stability. In contrast, the pristine NCM cathodes display dramatic capacity fading and more apparent decay with voltage, implying the serious degradation of crystal structure and aggravating parasitic reaction at the interface.

To explore the lithiation/delithiation performance, the first three cyclic voltammetry (CV) was performed at  $0.2 \text{ mV s}^{-1}$  over the voltage range of 3.0–4.5 V (Fig. 3c and d). All of the curves display an analogous shape and a pair of oxidation/reduction peaks appeared at around 3.7 V are attributed to the  $\text{Ni}^{2+}/\text{Ni}^{3+}$  redox, suggesting that the  $\text{LiNbO}_3$  coating does not in principle influence the charge/discharge. The parasitic reaction between the cathode and the electrolyte will form a passivation layer with low electron/ $\text{Li}^+$  kinetics at the interface and further increase the degree of polarization, which can be evaluated by the potential separation ( $\Delta E$ ) between anodic and cathodic peaks in the CV curves [36,37]. It is clearly measured that the  $\Delta E$  of NCM-LNO cathodes are 0.17 and 0.10 V in the first two cycles, that are all lower than these of pristine NCM cathodes (0.23 and 0.15 V). The smaller polarization in NCM-LNO cathodes benefits from the effective mitigation of interface parasitic reaction after coating modification. Furthermore, the better coincidence of NCM-LNO cathodes in the subsequent secondary lithiation process further demonstrates a preferable reversibility during the lithiation-delithiation process. The CV tests at diverse sweep rates from 0.4 to  $1.5 \text{ mV s}^{-1}$  were further carried out to research the  $\text{Li}^+$  diffusion dynamics, as displayed in Fig. S11. The fine linear relationship between the peak current ( $i_p$ ) and the square root of the scanning rate ( $v^{1/2}$ ) indicates the  $\text{Li}^+$  transfer in NCM cathodes exhibits a diffusion-controlled process (Fig. 3e and f) [38,39], and that the diffusion coefficients can be obtained according to the classical Randles-Sevcik equation (the details of calculation is shown in Supporting Information). Impressively, the  $\text{Li}^+$  diffusion coefficients of the NCM-LNO cathodes during the extraction/insertion process are  $2.63 \times 10^{-10} \text{ cm}^2 \text{ s}^{-1}$  and  $7.70 \times 10^{-11} \text{ cm}^2 \text{ s}^{-1}$ , which are all superior to the pristine NCM cathodes ( $1.38 \times 10^{-10} \text{ cm}^2 \text{ s}^{-1}/5.15 \times 10^{-11} \text{ cm}^2 \text{ s}^{-1}$ ). The enhancement of  $\text{Li}^+$  transfer kinetics is attributed to the construction of a homogeneous  $\text{LiNbO}_3$  coating, which reduces the generation of the electrochemical passivation layer by assuaging the surface parasitic reaction. Indeed, the  $\text{LiNbO}_3$  with high ionic conductivity ( $\sim 10^{-6} \text{ S cm}^{-1}$ ) can

further boost the  $\text{Li}^+$  transfer rate at the cathode-electrolyte interface.

To further clarify the impact of the  $\text{LiNbO}_3$  coating on the structural stability, the  $dQ/dV$  curves of various cycles acquired by differentiating charge–discharge curves are displayed in Fig. 4a and b. A couple of peaks appeared at  $\sim 3.7 \text{ V}$  correspond to the oxidation/reduction reaction during charging/discharging process, which coincides well with the results from the CV curves. The  $\text{LiNbO}_3$  coating layer can hinder the corrosion of electrolyte and stabilize the crystal structure, further improving the reversibility and reducing the polarization during consecutive cycling. Accordingly, the peaks in the NCM-LNO cathodes exhibit almost invariant positions (shifting just 0.03 V) and intensity over 100 cycles. However, the broadening and shifting toward higher values (0.11 V) after 100 cycles are observed for peaks in the pristine NCM cathodes. The polarization is also related to the kinetics of electrochemical reaction, so electrochemical impedance spectroscopy (EIS) was performed to further investigate the change of the interfacial impedance and reaction kinetics throughout the electrochemical cycling. As shown in Fig. 4c and d, both Nyquist plots contains two semicircles at the high and the medium frequency region, representing the surface film resistance ( $R_{sf}$ ) and the charge transfer resistance ( $R_{ct}$ ), respectively [39]. A tail at low frequency region is ascribed to Warburg impedance relevant to  $\text{Li}^+$  diffusion. The homologous circuits are also provided in the illustration. Specifically, the NCM-LNO cathodes display small  $R_{ct}$  of 34.3  $\Omega$ , 146.1  $\Omega$  and 221.6  $\Omega$  at 5th, 50th and 100th cycle, respectively, while the corresponding  $R_{ct}$  of pristine NCM cathodes are 65.7  $\Omega$ , 309.8  $\Omega$  and 613.2  $\Omega$ . The alleviation of an increase in EIS also implies a more stable interface due to the restricted parasitic reaction.

The change of surface chemical state of the NCM-LNO cathodes after electrochemical process was investigated by XPS with the NCM cathodes as a comparison. The intensities of all the XPS spectra were normalized. As depicted in C 1s peaks (Fig. 5a), the peaks at  $\sim 285 \text{ eV}$  represent the Super P (C–C), while the peaks of C–H and C–F located at  $\sim 286$  and  $\sim 290 \text{ eV}$  are both related to the PVDF binder [40]. Meanwhile, the peaks at  $\sim 287 \text{ eV}$  and  $288 \text{ eV}$  can be designated to ether and carbonate, which are attributed from electrolyte decomposition. Fig. 5b shows the F 1s spectra for both samples, and the peaks at  $\sim 684 \text{ eV}$ ,  $\sim 686 \text{ eV}$ , and  $\sim 687 \text{ eV}$  are assigned to  $\text{Li}_x\text{PO}_y\text{F}_z/\text{Li}_x\text{PF}_y$ , LiF, and PVDF [41,42]. The  $\text{Li}_x\text{PO}_y\text{F}_z/\text{Li}_x\text{PF}_y$  and LiF are products from electrolyte decomposition and parasitic reactions at the electrode/electrolyte interface. It is noteworthy that the peak intensities of carbon-oxygen compounds,  $\text{Li}_x\text{PO}_y\text{F}_z/\text{Li}_x\text{PF}_y$  and LiF in NCM-LNO cathodes are all lower than that of pristine NCM cathodes, suggesting less parasitic reactions and thinner cathode-electrolyte interphase (CEI) films. The more stable interface can also inhibit the dissolution of  $\text{Ni}^{4+}$ , and thus the dissolved Ni mass was also investigated by ICP-AES analysis of Li anode after 100 cycles [43,44]. As shown in Fig. S12, the dissolved Ni mass in the Li anode for NCM-LNO (1.1  $\mu\text{g}$ ) is lesser than that of pristine NCM (4.5  $\mu\text{g}$ ), directing evidencing the blocking of

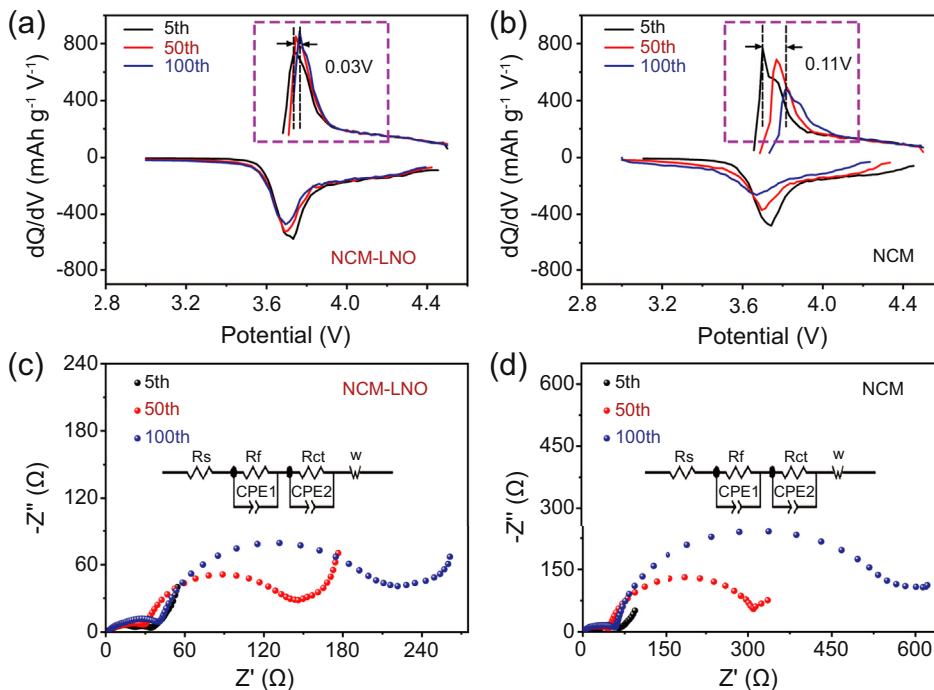


Fig. 4. (a, b) The calculated  $dQ/dV$  curves obtained by differentiating charge–discharge curves and (c, d) Nyquist plots of electrochemical impedances at the fully charged state (4.3 V) after different cycle numbers for the NCM-LNO and pristine NCM.

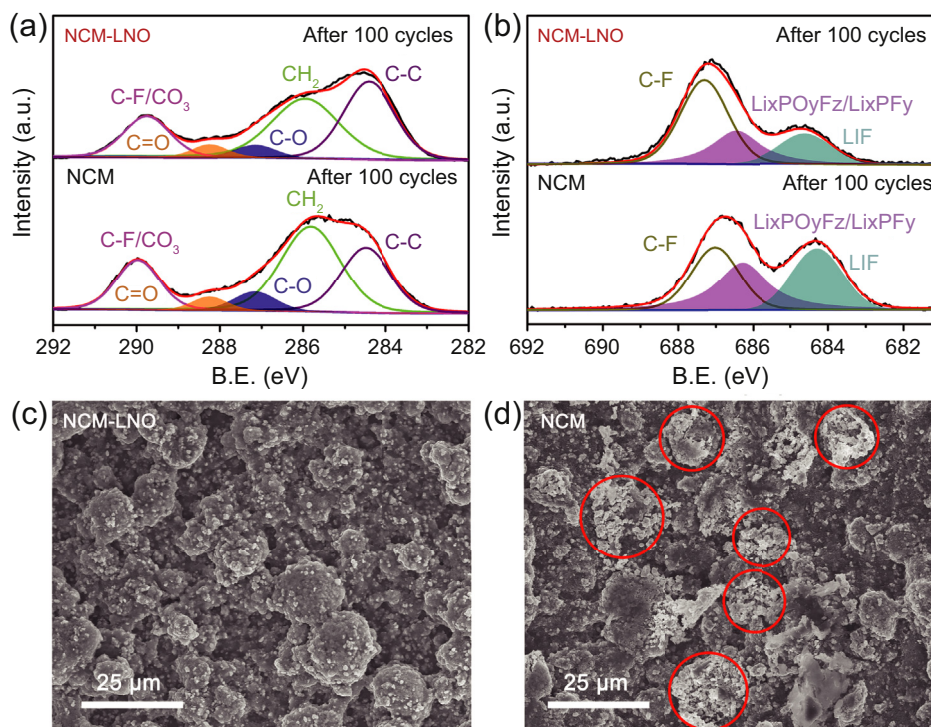


Fig. 5. (a, b) XPS spectra of C 1s and F 1s patterns, and (c, d) SEM images after 100 cycling of the NCM-LNO and pristine NCM.

$\text{Ni}^{4+}$  dissolution after  $\text{LiNbO}_3$  coating modification. To understand the function of coating layer on electrode morphology after long-term cycling, the SEM images of the NCM-LNO and pristine NCM cathodes after 100 cycles are

displayed in Fig. 5c and d. Compared to the integrated morphology of the NCM-LNO cathodes, the pristine NCM cathodes obviously show particle pulverization with severe cracks. It is widely accepted that the repetitive anisotropic

volume change of the primary particles during the delithiation/lithiation process will cause the intergranular crack, which can serve as fresh reaction sites to generate more destructive parasitic reactions with the electrolyte. The cumulative detrimental reactions will drastically undermine the surface structure and morphology of the pristine NCM cathode [36]. Therefore, the integrated morphology of the NCM-LNO cathodes proves that the  $\text{LiNbO}_3$  coating layer significantly reduces the penetration of the electrolyte and parasitic reactions at the interface, further stabilizing the morphology and slowing the reduction in capacity. Additionally, the particle pulverization can also destroy the electron/ $\text{Li}^+$  transfer inside the active materials to reduce the rate capability, so the complete morphology can also improve the rate performance. In conclusion, the tough and uniform  $\text{LiNbO}_3$  coating layer is advantageous for enhancing surface and consequently bulk structural stability and acts a critical role in high energy-power density NCM cathodes with enhanced life.

#### 4. Conclusions

In summary, we developed a citrate-assisted deposition concept to achieve a homogeneous  $\text{LiNbO}_3$  coating layer on a NCM523 surface that avoided self-nucleation and showed lithium conductivity. The  $\text{LiNbO}_3$  coating layer acted as a physical barrier can suppress electrolyte attack and the dissolution of metal ions, hence stabilizing the electrode-electrolyte interface. Moreover, the high  $\text{Li}^+$  conductivity of  $\text{LiNbO}_3$  can also significantly improve the  $\text{Li}^+$  diffusion kinetics and reduce electrode polarization during charging-discharging processes. As anticipated, the NCM-LNO cathodes exhibit outstanding Li-storage behavior including high capacity, enhanced rate capability and better cycling stability within the range 3.0–4.5 V. Specifically, the as-obtained NCM-LNO cathodes exhibit a specific capacity of  $207.4 \text{ mAh g}^{-1}$  at 0.2C and  $128.9 \text{ mAh g}^{-1}$  at 10C. Meanwhile, a 92% retention in capacity was realized after 100 cycles at 1C with smaller decline of voltage platform. The decreased side reaction and well-preserved morphology after 100 cycles further confirm the superior surface chemical stability and structure integrity of NCM-LNO cathodes. The surface engineering strategy proposed in this paper can also extended to various cathode materials that suffer from performance degradation propagating from the surface.

#### Conflict of interest

There are no conflicts of interest.

#### Acknowledgments

This work was supported by the National Natural Science Foundation of China (21975074, 91534202, and 91834301), the Shanghai Scientific and Technological Innovation Project (18JC1410500), and the Fundamental Research Funds for the Central Universities (222201718002).

#### Appendix A. Supplementary data

Supplementary data to this article can be found online at <https://doi.org/10.1016/j.gee.2020.09.011>.

#### References

- [1] J.M. Tarascon, M. Armand, *Nature* 414 (2011) 359–367.
- [2] R. Weber, M. Genovese, A. Louli, S. Hames, C. Martin, I. Hill, J. Dahn, *Nat. Energy* 4 (2019) 683–689.
- [3] H. Zhao, B. Qiu, H.C. Guo, K. Jia, Z.P. Liu, Y.G. Xia, *Green Energy Environ.* 2 (2017) 174–185.
- [4] W. Li, E. Erickson, A. Manthiram, *Nat. Energy* 5 (2020) 26–34.
- [5] J. Kim, H. Lee, H. Cha, M. Yoon, M. Park, J. Cho, *Adv. Energy Mater.* 8 (2018) 1702028.
- [6] J.A. Gilbert, J. Barendo, D.P. Abraham, *J. Electrochem. Soc.* 164 (2017) A6054–A6065.
- [7] W. Li, B. Song, A. Manthiram, *Chem. Soc. Rev.* 46 (2017) 3006–3059.
- [8] J. Shi, D. Xiao, M. Ge, X. Yu, Y. Chu, X. Huang, X. Zhang, Y. Yin, X. Yang, Y. Guo, L. Gu, L. Wan, *Adv. Mater.* 9 (2018) 1705575.
- [9] S. Jung, H. Gwon, J. Hong, K. Park, D. Seo, H. Kim, J. Hyun, W. Yang, K. Kang, *Adv. Energy Mater.* 4 (2014) 1300787.
- [10] Y. Ruan, X. Song, Y. Fu, C. Song, V. Battaglia, *J. Power Sources* 400 (2018) 539–548.
- [11] H. Kim, M.G. Kim, H.Y. Jeong, H. Nam, J. Cho, *Nano Lett.* 15 (2015) 2111–2119.
- [12] S. Li, X. Fu, J. Zhou, Y. Han, P. Qi, G. Xing, F. Xiao, W. Bo, *J. Mater. Chem.* 4 (2016) 5823–5827.
- [13] H. Kim, S. Lee, H. Cho, J. Kim, J. Lee, S. Park, S. Joo, S. Kim, Y. Cho, H. Song, S. Kwak, J. Cho, *Adv. Mater.* 28 (2016) 4705–4712.
- [14] H.F. Yu, Y.G. Li, Y.J. Hu, H. Jiang, C.Z. Li, *Ind. Eng. Chem. Res.* 58 (2019) 4108–4115.
- [15] H.W. Zhu, H.F. Yu, H. Jiang, Y.J. Hu, H.B. Jiang, C.Z. Li, *Chem. Eng. Sci.* 217 (2020) 115518.
- [16] H. Jiang, Y.S. Han, Q. Zhang, J.X. Wang, Y. Fan, C.Z. Li, *Rev. Chem. Eng.* 35 (2019) 917–927.
- [17] Y. Su, S. Cui, Z. Zhuo, W. Yang, X. Wang, F. Pan, *ACS Appl. Mater. Interfaces* 7 (2015), 25205–25112.
- [18] Y. Cho, Y. Lee, S. Park, Y. Lee, J. Cho, *Electrochim. Acta* 1 (2010) 333–339.
- [19] S. Lee, C. Yoon, K. Amine, Y. Sun, *J. Power Sources* 234 (2013) 201–207.
- [20] R. Qi, J. Shi, X. Zhang, X. Zeng, Y. Yin, J. Xu, L. Chen, W. Fu, Y. Guo, L. Wan, *Sci. China Chem.* 60 (2017) 1230–1235.
- [21] H.G. Song, J.Y. Kim, K.T. Kim, Y.J. Park, *J. Power Sources* 196 (2011) 6847–6855.
- [22] N. Ohta, K. Takada, I. Sakaguchi, L.Q. Zhang, R.Z. Ma, K. Fukuda, M. Osada, T. Sasaki, *Electrochem. Commun.* 9 (2007) 1486–1490.
- [23] W. Sun, M. Xie, X.X. Shi, L.Q. Zhang, *Mater. Res. Bull.* 61 (2015) 287–291.
- [24] Z.J. Zhang, S.L. Chou, Q.F. Gu, H.K. Liu, H.J. Li, K. Ozawa, J.Z. Wang, *ACS Appl. Mater. Interfaces* 6 (2014) 22155–22165.
- [25] M. Gellert, K.I. Gries, J. Sann, E. Pfeifer, K. Volz, B. Roling, *Solid State Ionics* 287 (2016) 8–12.
- [26] X.L. Li, L.B. Jin, D.W. Song, H.Z. Zhang, X.X. Shi, Z.Y. Wang, L.Q. Zhang, L.Y. Zhu, *J. Energy Chem.* 40 (2020) 39–45.
- [27] Y.J. Kim, R. Rajagopal, S. Kang, K.S. Ryu, *Chem. Eng. J.* 386 (2020) 123975.
- [28] H. Kim, D. Byun, W. Chang, H.G. Jung, W.C. Choi, *J. Mater. Chem.* 5 (2017) 25077–25089.
- [29] G.Z. Shang, Y.W. Tang, Y.Q. Lai, J. Wu, X. Yang, H.X. Li, C. Peng, J.F. Zheng, Z.A. Zhang, *J. Power Sources* 423 (2019) 246–254.
- [30] S. Kang, J. Kim, M. Stoll, D. Abraham, Y. Sun, K. Amine, *J. Power Sources* 112 (2002) 41–48.
- [31] R. Zheng, W. Wang, Y. Dai, Q. Ma, Y. Liu, D. Mu, R. Li, J. Ren, C. Dai, *Green Energy Environ.* 2 (2017) 42–50.
- [32] Y. Chen, S. Tang, S. Deng, T. Lei, Y. Li, W. Li, G. Cao, J. Zhu, J. Zhang, *J. Power Sources* 431 (2019) 8–16.

- [33] X. Zheng, X. Li, Z. Wang, H. Guo, Z. Huang, G. Yan, D. Wang, *Electrochim. Acta* 191 (2016) 832–840.
- [34] H. Liu, Y. Yang, J. Zhang, *J. Power Sources* 162 (2006) 644–650.
- [35] S. Liu, X. Chen, J. Zhao, J. Su, C. Zhang, T. Huang, J. Wu, A. Yua, *J. Power Sources* 374 (2018) 149–157.
- [36] Y. Wu, H. Ming, M. Li, J. Zhang, W. Wahyudi, L. Xie, X. He, J. Wang, Y. Wu, J. Ming, *ACS Energy Lett.* 4 (2019) 656–665.
- [37] Q.Q. Jiang, H.F. Yu, Y.J. Hu, H. Jiang, C.Z. Li, *Ind. Eng. Chem. Res.* 58 (2019) 23099–23105.
- [38] L. Chen, H. Jiang, Y. Hu, H. Wang, C. Li, *Sci. China Mater.* 61 (2018) 1049–1056.
- [39] Y. Li, H. Yu, Y. Hu, H. Jiang, C. Li, *J. Energy Chem.* 2 (2018) 559–564.
- [40] Y. Li, S. Wan, G.M. Veith, R.R. Unocic, M.P. Paranthaman, S. Dai, X.G. Sun, *Adv. Energy Mater.* 7 (2017) 1601397.
- [41] M. Xu, L. Zhou, Y. Dong, Y. Chen, J. Demeaux, A.D. MacIntosh, A. Garsuch, B.L. Lucht, *Energy Environ. Sci.* 9 (2016) 1308–1319.
- [42] Y. Che, X. Lin L. Xing, X. Guan, R. Guo, G. Lan, Q. Zheng, W. Zhang, W. Li, *J. Energy Chem.* 52 (2021) 361–371.
- [43] J.Y. Li, W.D. Li, Y. You, A. Manthiram, *Adv. Energy Mater.* 8 (2018) 1801957.
- [44] W. Liu, J. Li, W. Li, H.Y. Xu, C. Zhang, X.P. Qiu, *Nat. Commun.* 11 (2020) 3629.